PAPER

Check for updates

Lumino-structural properties of Dy^{3+} activated Na$_3$Ba$_2$LaNb$_{10}$O$_{30}$ phosphors with enhanced internal quantum yield for w-LEDs

Kanishk Poria, [iD] [a] Ravina Lohan,[b] Sanjana Bhatia,[a] Amit Kumar,[b] Rajwinder Singh,[a] Nisha Deopa, [iD] *[b] Rajesh Punia,[c] Jangvir Singh Shahi*[a] and A. S. Rao[d]

With an intend to develop white light emitting phosphor, for w-LED application, a series of dysprosium (Dy^{3+}) doped novel Na$_3$Ba$_2$LaNb$_{10}$O$_{30}$ phosphors were prepared using solid state reaction technique at 1300 °C. Their structural, morphological and vibrational spectroscopic analysis was performed. We illustrate the luminescence characteristics of the prepared phosphors for various Dy^{3+} ion doping concentration. The XRD analysis demonstrates that the prepared phosphors were in single phase, and of tetragonal tungsten bronze structure of the *P4bm* space group. The FE-SEM image reveals that the prepared phosphors contained irregular shaped both nano and micro particles. Under near-ultraviolet (n-UV) irradiation at 387 nm, the photoluminescence (PL) emission spectra shows three characteristic bands at 481 nm (blue), 575 nm (yellow) and 666 nm (red). Obtained optimized Dy^{3+} ion concentration for the prepared sample is 7.0 mol%, beyond which the concentration quenching begins. Bonding between Dy–O is covalent in nature as confirmed by bonding parameters and the Dexter theory revealed that the energy transfer among Dy^{3+} ions is dipole–diploe interaction. CIE chromaticity coordinates, CCT and color purity confirms the formation of warm white light emitting phosphors. Lifetime analysis demonstrates the longer decay time in the phosphors. The Internal Quantum Yield (IQE) and brightness (*B*) for the optimised phosphor is calculated as 45.35% and 11.41% respectively, which makes it a suitable phosphor for w-LED.

1 Introduction

Phosphor is any material that exhibits the phenomenon of luminescence when subjected to UV radiation, X-rays, electron bombardment, friction or any other form of excitation. A phosphor primarily comprises of a host matrix and an activator ion in its lattice.[1] These activators act as the luminescent centres, *i.e.* the electron relaxes radiatively at this activator site, within the host matrix. Rare earth elements such as Eu^{3+}, Eu^{2+}, Dy^{3+}, Pr^{3+} are few example of activators. Phosphors are used, in the creation of several optoelectronic devices, including light converters, solid state lasers, solid state lighting, optical thermometer and optical amplifiers, *etc.*[2–7] In the last decade, phosphor-converted white light emitting diodes (pc-wleds) have been studied significantly owing to their key characteristic, such as efficient light output, low power consumption, longer operational lifetime (>100 000 hours), sturdiness and

environmentally safer as compared to their predecessors, fluorescent and incandescent lamp.[8–12] Nowadays, w-LEDs are widely used in plant cultivation (including vegetables, flowers, herbs, *etc.*), display, medical lighting, and outdoor lighting.[13–15]

White light emission can be obtained in three ways from solid state lighting sources.[16,17] The first way is to setup an array of multiple LED chips emitting light at different frequencies. Multiple LED setup has excellent colour rendering index and the white point can be easily controlled. However, there is no control on correlated colour temperature, since each LED needs an independent output power control and has its own different lifetime. The second way is to use a single UV LED chip coated with a combination of red, green and blue down-converting phosphors. This setup is quite cost efficient than LED matrix, as it gives excellent colour rendering and a control over white light-CCT. Because of stokes conversion, this approach becomes less energy efficient, and it is difficult to manage the homogeneity of the phosphor coating. Another demerit is that phosphors deteriorate faster than LEDs. The third way is utilizing a single LED (blue) with a coating of yellow down-converting phosphor. The blue light bleeds through the phosphor to give white light. This setup is small, light-weight, easy to operate and has a long lifetime. Demerit of this setup is that it is

[a]*Department of Physics, Panjab University, Chandigarh, India. E-mail: shahijs@yahoo.com; Tel: +91-9815612645*

[b]*Department of Physics, Chaudhary Ranbir Singh University, Jind, India. E-mail: nispectro999@gmail.com; Tel: +91-8860551723*

[c]*Department of Physics, Maharshi Dayanand University, Rohtak, India*

[d]*Department of Applied Physics, Delhi Technological University, New Delhi, India*

less efficient because of stokes shift and has a very poor colour rendering.

Since niobates have better chemical and physical stability, they make excellent luminous matrixes. Some rare-earth ion doped niobates, such as $Sr_2LaNbO_6:Eu^{3+},Sm^{3+}$; $LaNbO_4:Bi^{3+}/Dy^{3+}$ and $Ca_2LaNbO_6:Sm^{3+}$, have been shown to exhibit outstanding luminous characteristics along with high thermal stability.[18–20] It is important to note that the tungsten bronze structure (TTB) exhibits chemical and magnetic stability with excellent crystal structure. Niobates having TTB structures are excellent candidates for ferroelectric and piezoelectric materials. The deficient perovskite TTB niobates consist of corner-sharing NbO_6 octahedra arrays and three different tunnels for cation filling, leading to large spontaneous polarization and high dielectric constants.[21] In deformed metal–oxygen polyhedra, they likewise show dominating electron–hole separation and transport through static electric fields between structure-induced dipole moments. As a result, a little structural change such as changing the cation-site occupancy has a huge influence on charge mobility. Utilising this property, we have opted to use niobate based TTB structure to investigate its photoluminescence properties. Moreover, the tungsten bronze phosphors such as $Sr_5YTi_3Nb_7O_{30}$, $NaSr_2Nb_5O_{15}$ and $Ba_4LaTiNb_9O_{30}$ have been reported to have potential applications in photonics, especially in w-LED.[22–24] The tetragonal tungsten bronze structure has been shown to readily accept lanthanides or transition metals as constituents or dopants because of its tetragonal crystal structure, which enables the manufacture of high-quality doped single crystals.[25] The general practice to prepare niobate-based phosphors is the solid state reaction method, which has the benefit of producing samples with excellent morphology and luminosity, over other methods.[26]

In search of a suitable host lattice, scientists have been conducting research in order to prepare phosphor-converted white light emitting diode (pc-wled).[27] In our present study, we focus towards the generation of white light from dysprosium doped $Na_3Ba_2LaNb_{10}O_{30}$ phosphors via solid state reaction technique. We examine the structure parameter, surface morphology and elemental analysis of the as prepared phosphors using the X-ray diffraction (XRD), field emission scanning electron microscopy (FESEM) and energy dispersive X-ray spectroscopy (EDX), respectively. Further, optical properties were examined employing the steady-state and time resolved photoluminescence.
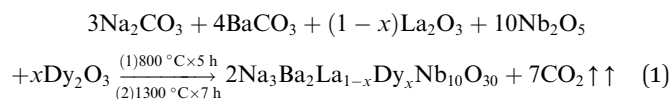
Generally, Dy^{3+} ions exhibit three emission bands in the visible spectra, the blue emission (450–490 nm) corresponds to $^4F_{9/2} \rightarrow {^6}H_{15/2}$ transition, yellow emission (550–590 nm) corresponds to $^4F_{9/2} \rightarrow {^6}H_{13/2}$ hypersensitive transition and the red emission (640–680 nm) corresponds to $^4F_{9/2} \rightarrow {^6}H_{11/2}$ transition, latter being a feeble transition.[28–30]

2 Experimental procedure

2.1 Phosphor preparation

The samples of dysprosium doped niobate-based $Na_3Ba_2LaNb_{10}O_{30}:xDy^{3+}$ ($x = 0, 1, 3, 5, 7$ and 10 mol%) phosphors have been synthesized via high-temperature solid-state reaction

technique. The raw materials Na_2CO_3 (99.5%), $BaCO_3$ (99.9%), La_2O_3 (99.9%), Dy_2O_3 (99.9%) and Nb_2O_5 (99.9%) used for the synthesis were of Sigma Aldrich and analytical grade quality. The precursor were taken in their stoichiometric ratios and were thoroughly mixed and milled together in a mortar and pestle for 2 hours. The grounded samples were subsequently calcinated at a heating rate of 3 °C min^{-1}, in a programmable muffle furnace of Metrex Scientific Instruments (Model: MF-14P). The heating process consisted of two steps. The reaction time for the first step of calcination was 5 hours at 800 °C and the second step was 1300 °C for 7 hours. Finally the samples were rigorously grounded to make a fine powder and the phosphorescence for the optimised sample (7 mol%) can be easily seen in Fig. 1. The chemical reaction involved in this process is shown in eqn (1).

$$3Na_2CO_3 + 4BaCO_3 + (1-x)La_2O_3 + 10Nb_2O_5$$
$$+ xDy_2O_3 \xrightarrow[\text{(2)}1300\,°C \times 7\,h]{\text{(1)}800\,°C \times 5\,h} 2Na_3Ba_2La_{1-x}Dy_xNb_{10}O_{30} + 7CO_2\uparrow\uparrow \quad (1)$$

2.2 Characterization techniques

The structural parameter of the prepared phosphors were investigated by XRD analysis using Panalytical model X'pert Pro with Cu-K$_\alpha$ radiation ($\lambda = 1.5406$ Å) in the 2θ range from 20° to 80°. The surface morphology, energy dispersive spectroscopy (EDS), and elemental mapping of the prepared samples were investigated by FESEM. A thin layer of gold (Au) was coated on the as-synthesized samples and were analysed using FESEM utilising JEOL JSM-6490 operated at the accelerating voltage of 5 kV. The Fourier transform infrared (FT-IR) spectrum of $Na_3Ba_2LaNb_{10}O_{30}$ were recorded using a PerkinElmer Frontier Spectrometer in the middle infrared region (4000–400 cm^{-1}) after the pellets were prepared by mixing the samples with potassium bromide (KBr_2, A.R. grade) and then compressed using a hydraulic press at 10 ton load. The steady state photoluminescence spectra (PL) of the prepared phosphors were recorded using Cary Eclipse Fluorescence Spectrophotometer. The lifetime decay spectra has been studied using Horiba Spectroscope excited through a 150 watts microsecond xenon
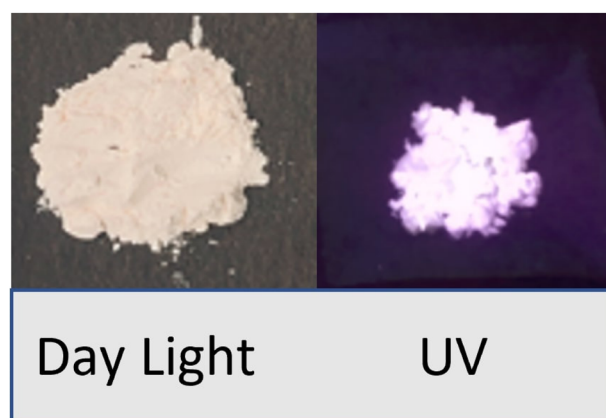

Fig. 1 Image of $Na_3Ba_2LaNb_{10}O_{30}:xDy^{3+}$ ($x = 7$ mol%) phosphor sample under daylight and 365 nm UV light.

flash lamp. The excitation and emission spectra was collected in the range of 320–470 nm and 400–700 nm, respectively. The internal quantum efficiency (IQE) was collected by Horiba Scientific QuantaPhi-2 equiped with an integrating sphere coated with $BaSO_4$. Commission international de l'Eclairage (CIE) 1931 chromaticity coordinates were calculated and plotted for the emission spectra. All measurements were carried out at room temperature.

3 Results and discussion

3.1 X-ray diffraction and structural analysis

The powder X-ray diffraction (XRD) analysis demonstrated the crystal structure of $Na_3Ba_2LaNb_{10}O_{30}{:}xDy^{3+}$ (x = 0, 1, 3, 5, 7 and 10 mol%) phosphors and matches well with the JCPDS card no. 00-038-1236 corresponding to $Na_3Ba_2LaNb_{10}O_{30}$, as shown in Fig. 2. XRD peaks reveals that the inclusion of dysprosium ion does not effect the crystal structure of $Na_3Ba_2LaNb_{10}O_{30}$. Furthermore, the crystal structure of $Na_3Ba_2LaNb_{10}O_{30}{:}xDy^{3+}$ (x = 0, 1, 3, 5, 7 and 10 mol%) phosphor belongs to the filled tetragonal tungsten bronze (TTB) structure of the $P4bm$ space group. The general representation of tungsten bronze structure is $[(A_1)_2(A_2)_4]C_4[(B_1)_2(B_2)_8]O_{30}$. It can be seen that the TTB structure consists of three different crystal sites namely six A sites, ten B sites (B crystal sites are located in the center of the $[BO_6]$ octahedrons), and the triangular interstitial C site (mostly

empty).[31] In the present study of $Na_3Ba_2LaNb_{10}O_{30}{:}xDy^{3+}$ (x = 0, 1, 3, 5, 7 and 10 mol%), Ba^{2+} and La^{3+} present at two A_1 crystal sites while Na^{1+} and Ba^{2+} are present at four A_2 crystal sites whereas Nb^{5+} occupies all ten B sites. In order to figure out which element of the matrix is swapped with Dy^{3+} ion, the ionic radii percentage difference (D_r) is calculated and reproduced using the following expression.[32]

$$D_r = \frac{R_s(CN) - R_d(CN)}{R_s(CN)} \times 100\% \qquad (2)$$

where, R_s and R_d are the ionic radii of the cation in the matrix and doped Dy^{3+} ion respectively. The ionic radii of cations that corresponds to the coordination number six are $Na^{1+}(R_s = 1.02$ Å), $Ba^{2+}(R_s = 1.35$ Å), $La^{3+}(R_s = 1.032$ Å), $Nb^{5+}(R_s = 0.64$ Å) and doped ion $Dy^{3+}(R_d = 0.912$ Å). The calculated D_r values are 10.59%, 32.44%, 11.63% and −42.5% respectively. Among all the cations, Na^{1+} and La^{3+} are the closest ions to be replaced by the Dy^{3+} ion. Since both La and Dy exist in trivalent oxidation state, Dy^{3+} ions would occupy the site of La^{3+} ion. Dy^{3+} will not substitute Na^{1+} as it leads to chemically nonequivalent substitution and the host lattice acquires an excess positive charge.

The Debye–Scherrer formula (eqn (3)) is employed to compute the average crystallite size of the prepared phosphors.[33,34]

$$D = \frac{K\lambda}{\beta \cos \theta} \qquad (3)$$

where K is the form factor (usually 0.94), λ denotes the X-ray wavelength (1.5406 Å, for Cu-K_α), θ represents the Braggs diffraction angle and β denotes the FWHM (full-width at half maxima). For $Na_3Ba_2LaNb_{10}O_{30}{:}xDy^{3+}$ (x = 0, 1 and 10 mol%) phosphor, the average crystallite size is summarized in Table 1. The results show that as the Dy^{3+} ion concentration increased the D value declines.

A very slight shift (of the order of 10^{-2} Å) in the 2θ angle of the most intense peak of $Na_3Ba_2LaNb_{10}O_{30}$ ((311) plane) is observed to shift towards the higher 2θ angle as we increase the doping concentration. This propensity may be brought on by the mismatch between the ionic radii of Dy^{3+} and La^{3+} ions, which further raises the possibility of Dy^{3+} ion incorporation into $Na_3Ba_2LaNb_{10}O_{30}$. This slight shift can be easily seen from Fig. 3.

3.2 Field emission scanning electron microscopy and energy dispersive X-ray spectroscopy

Surface morphology of the prepared $Na_3Ba_2LaNb_{10}O_{30}{:}xDy^{3+}$ (x = 7 mol%) phosphor is obtained using FE-SEM depicted in
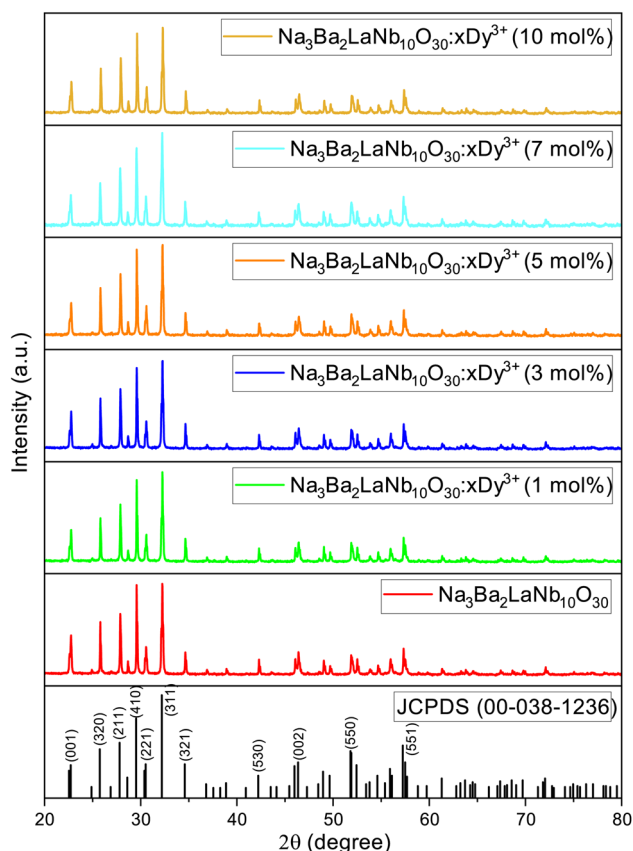
Fig. 2 XRD patterns of JCPDS 00-038-1236 and $Na_3Ba_2LaNb_{10}$-$O_{30}{:}xDy^{3+}$ (x = 0, 1, 3, 5, 7 and 10 mol%) phosphors.

Table 1 Crystallite size of $Na_3Ba_2LaNb_{10}O_{30}{:}xDy^{3+}$ (x = 1, 3, 5, 7 and 10 mol%) phosphors

Dy^{3+} (mol%)	Average crystallite size, D (nm)
0.0	41.45057
1.0	40.35571
10.0	40.25051
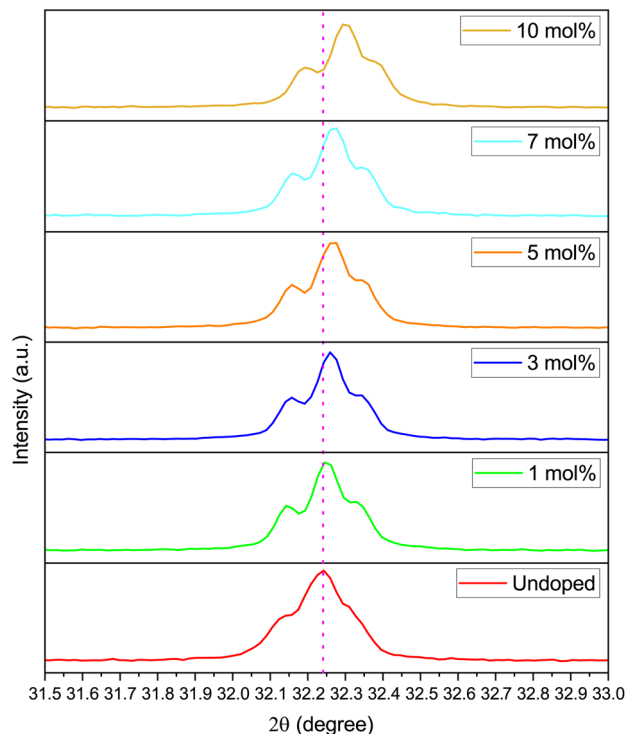
Fig. 3 XRD peak corresponding to 311 plane of $Na_3Ba_2LaNb_{10}O_{30}$:-xDy^{3+} (x = 0, 1, 3, 5, 7 and 10 mol%) phosphors.

Fig. 4. From FE-SEM images, the phosphor particles were inferred as non-uniform, inhomogeneous and irregular in shape. The agglomeration of particles were expected in the preparation of phosphor through high-temperature solid state reaction method. The agglomerated particle size range from few micrometers to few nanometers, and are tightly packed with each other. Because of the large surface area to volume ratio, number of voids are observed inside the agglomerated nano-particles. No change in the morphology is observed with the change in dopant ion concentrations.

The EDX spectrum and elemental mapping reveals the chemical composition and elemental distribution in the

Fig. 5 EDX spectrum of $Na_3Ba_2LaNb_{10}O_{30}$:xDy^{3+} (x = 7 mol%) phosphor.

prepared $Na_3Ba_2LaNb_{10}O_{30}$:xDy^{3+} (x = 7 mol%) phosphor. EDX is a typical approach for detecting and measuring the qualitative and quantitative elemental composition of a sample in an area of few square nanometer dimensions. The elemental peaks corresponding to sodium (Na), barium (Ba), lanthanum (La), niobium (Nb), oxygen (O) and dysprosium (Dy) of the prepared sample was observed in the EDX spectrum and are shown in Fig. 5. Their elemental mapping is demonstrated in Fig. 6 which depicts the even distribution of constituent elements. The atomic% shown in Fig. 5 also confirms the agglomeration of $Na_3Ba_2LaNb_{10}O_{30}$:xDy^{3+} (x = 7 mol%) doped phosphor.

3.3 Raman and Fourier transform infrared spectroscopy

Raman spectra of the synthesized $Na_3Ba_2LaNb_{10}O_{30}$:xDy^{3+} (x = 7 mol%) phosphor in the tetragonal structure, with the octahedral ion $[NbO_6]^{7-}$, recorded at room temperature from 100–1000 cm^{-1} wavenumber as shown in Fig. 7. The three Raman

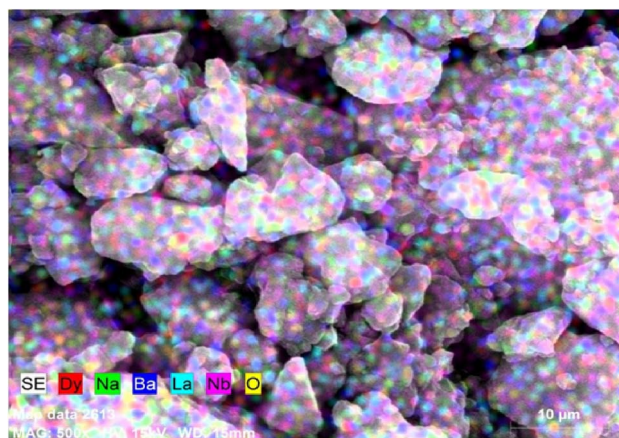**Fig. 4** FE-SEM micrograph of $Na_3Ba_2LaNb_{10}O_{30}$:xDy^{3+} (x = 7 mol%) phosphor sintered at 1300 °C.

Fig. 6 Elemental mapping of $Na_3Ba_2LaNb_{10}O_{30}$:xDy^{3+} (x = 7 mol%) phosphor.
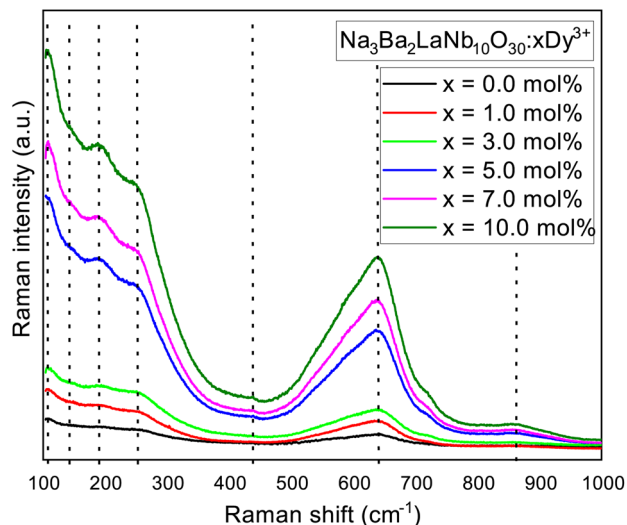
Fig. 7 Raman spectrum of $Na_3Ba_2LaNb_{10}O_{30}$:xDy^{3+} ($x = 0$, 1, 3, 5, 7 and 10 mol%) phosphor at room temperature.
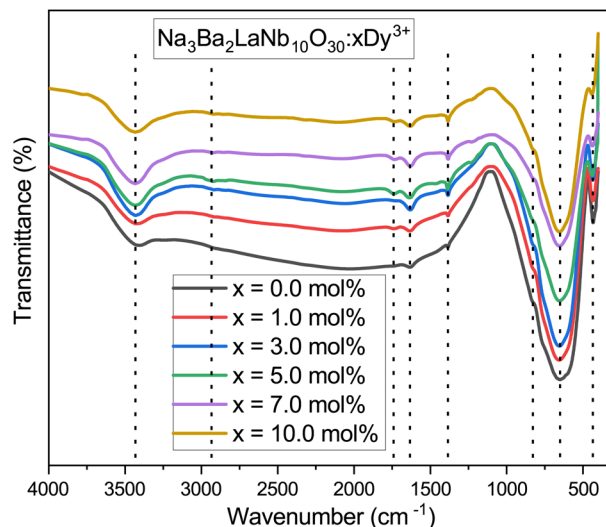
Fig. 8 Fourier transformed infrared (FT-IR) spectrum of Na_3Ba_2-$LaNb_{10}O_{30}$:xDy^{3+} ($x = 0$, 1, 3, 5, 7 and 10 mol%) phosphor at room temperature.

active modes centered at 252 cm^{-1} (ν_5) corresponds to O–Nb–O bend vibrations, 639 cm^{-1} (ν_2) assign to Nb–O stretch vibrations, and 862 cm^{-1} (ν_1) corresponds to Nb–O stretch vibrations, is similar to one other in tetragonal tungsten bronze structure with the point group C_{4v} (ref. 35 and 36) and C_{2v}.[37] For the tungsten bronzes structure, all Raman lines except for the three characteristic vibrational modes originate from the external vibrations for oxygen octahedron. Therefore, the Raman spectra of $Na_3Ba_2LaNb_{10}O_{30}$ can be discussed in terms of internal vibrations of the (NbO_6) octahedra and external vibrations involving the motions of Na^{1+}, Ba^{2+} and La^{3+} cations. As shown in Fig. 7, the peaks centered at 108 cm^{-1}, 142 cm^{-1}, 189 cm^{-1} and 438 cm^{-1} originate from external vibration modes.

The FT-IR spectra are recorded from 4000–400 cm^{-1} wavenumber to know about the structural units and functional groups in the as-prepared $Na_3Ba_2LaNb_{10}O_{30}$:xDy^{3+} ($x = 1$, 3, 5, 7 and 10 mol%) phosphor. Fig. 8 depicted the FT-IR spectra of as-synthesized phosphor. The quality of product is best checked by the FT-IR spectroscopy and is used in the initial stage process for the analysis of material. The shift in the peaks of spectra suggests the inclusion of contaminate. All the spectra shows similar shoulder positions as demonstrated in the Fig. 8. FT-IR spectra contain eight shoulders about 435, 654, 829, 1386, 1633, 1743, 2921 and 3432 cm^{-1}. The shoulders in the spectra are assigned according to the previously published research papers. The shoulder near 435 and 829 cm^{-1} consigned to the coupling between Nb–O stretching mode.[38] The shoulder about 654 cm^{-1} is owing to the La–O stretching vibrations.[39] The shoulder about 1386 cm^{-1} is because of symmetric stretching of COO^- functional group.[40] The shoulder in the region 1633 and 3432 cm^{-1} is because of water molecules.[41] The shoulder near 1743 cm^{-1} is contributed by C–O stretching mode in free carboxylic group.[42] The shoulder about 2921 cm^{-1} may correspond to the residual organic presence.[43]

3.4 Bandgap and electronic structure

Using reflectance spectra we can explore optical characteristics of phosphors. Bandgap (E_g) of $Na_3Ba_2LaNb_{10}O_{30}$:xDy^{3+} ($x = 1$, 3, 5, 7 and 10 mol%) phosphor samples can be calculated using Tauc plot[44] derived from the plot of diffuse reflectance spectra of the phosphors. Fig. 9 exhibit UV-Vis diffuse reflectance spectra of $Na_3Ba_2LaNb_{10}O_{30}$:xDy^{3+} ($x = 1$, 3, 5, 7 and 10 mol%) phosphor and Fig. 10 shows the corresponding Tauc plot determined from eqn (4). The transition $^6H_{15/2} \rightarrow {}^6F_{5/2}$ and $^6H_{15/2} \rightarrow {}^6F_{7/2}$ at 808 nm and 908 nm, respectively can be easily seen in Fig. 9.

$$(\alpha_{abs} h\nu_{ph})^n = A(h\nu_{ph} - E_g) \tag{4}$$

where A represents a constant, α_{abs} denotes the absorption coefficient, ν_{ph} represents the photon frequency and n is the transition dependent parameter ($n = 1/2$ corresponds to
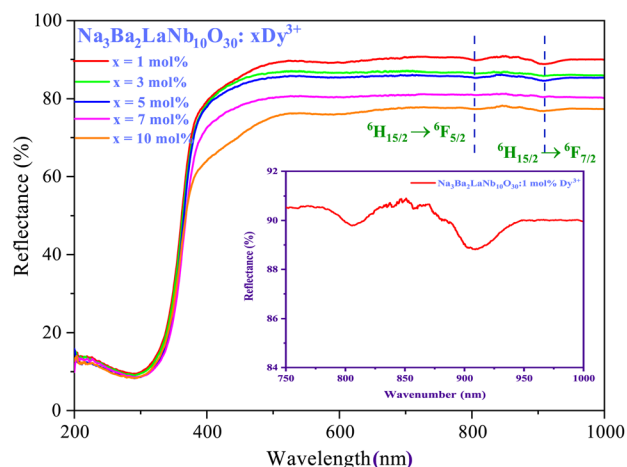

Fig. 9 Diffuse reflectance spectra of $Na_3Ba_2LaNb_{10}O_{30}$:xDy^{3+} ($x = 1$, 3, 5, 7 and 10 mol%) phosphor.
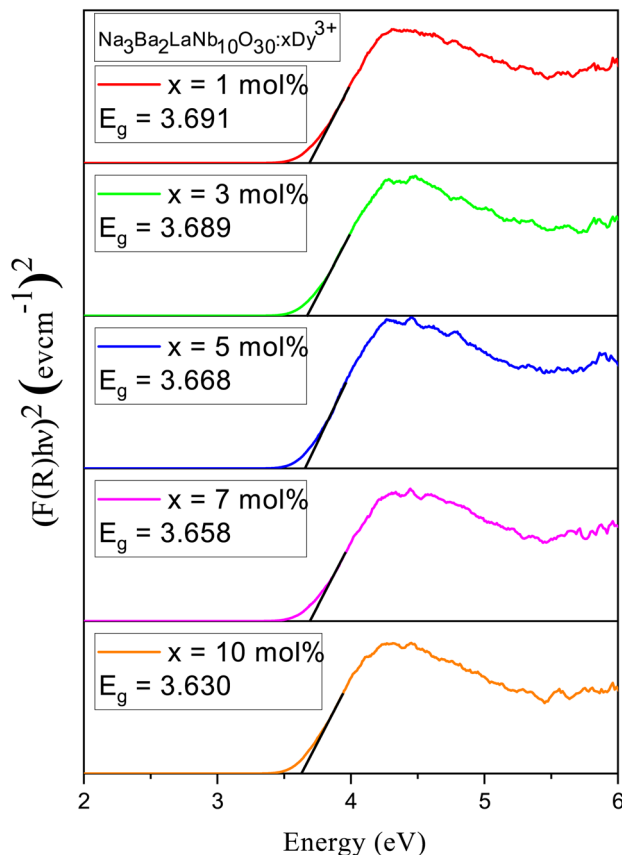
Fig. 10 Tau plot of un-doped and $Na_3Ba_2LaNb_{10}O_{30}$:xDy^{3+} ($x = 1, 3, 5, 7$ and 10 mol%) phosphors for the determination of optical bandgap E_g (assuming indirect transitions).

allowed electronic transition (direct), $n = 2$ for allowed electronic transition (indirect), while $n = 3/2$ and 3 corresponds to forbidden direct and indirect electronic transition, respectively). A red shift is represented in the optical bandgap of the $Na_3Ba_2LaNb_{10}O_{30}$:xDy^{3+} ($x = 1, 3, 5, 7$ and 10 mol%) phosphor with increase in Dy^{3+} ion concentration, as seen in Fig. 10. Table 2 shows the bandgap for $Na_3Ba_2LaNb_{10}O_{30}$:xDy^{3+} ($x = 1, 3, 5, 7$ and 10 mol%) phosphor.

3.5 Steady state photoluminescence

The photoluminescence excitation (PLE) spectra of dysprosium doped niobate-based $Na_3Ba_2LaNb_{10}O_{30}$:xDy^{3+} ($x = 1, 3, 5$ and 10 mol%) phosphors are demonstrated in Fig. 11, which were

Table 2 Bandgap, nephelauxetic ratio (β) and bonding parameter (δ) in $Na_3Ba_2LaNb_{10}O_{30}$:xDy^{3+} ($x = 1, 3, 5, 7$ and 10 mol%) phosphors

Dy^{3+} (mol%)	Bandgap (eV)	Nephelauxetic Ratio (β)	Bonding Parameter (δ)
1.0	3.691	0.99980	0.00021
3.0	3.689	0.99973	0.00028
5.0	3.668	0.99938	0.00062
7.0	3.658	0.99883	0.00117
10.0	3.630	0.99601	0.00401
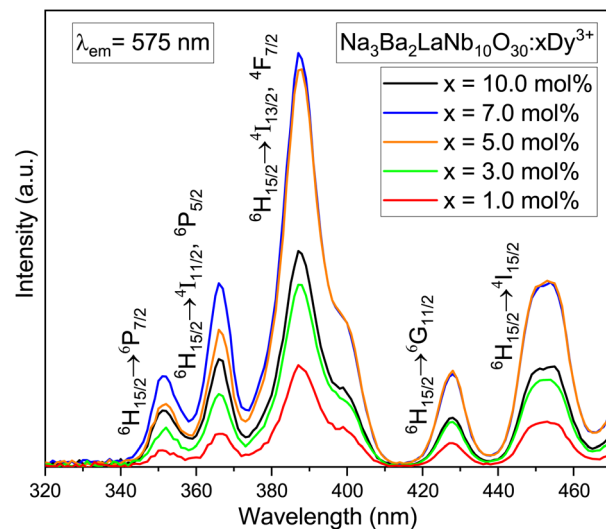
Fig. 11 PLE spectra of $Na_3Ba_2LaNb_{10}O_{30}$:xDy^{3+} ($x = 1, 3, 5, 7$ and 10 mol%) phosphors by fixing emission at 575 nm.

performed in wavelength range 320–470 nm for fixed emission wavelength of 575 nm. Several excitation peaks were observed at 351, 366, 387, 427 and 453 nm due to the characteristic Dy^{3+} ion transitions from $^6H_{15/2}$ (ground state) to several excited states as exhibited in Fig. 15. The five intense peaks correspond to $^6H_{15/2} \rightarrow {}^6P_{7/2}$(351 nm); $^6H_{15/2} \rightarrow {}^4I_{11/2}$, $^6P_{5/2}$(366 nm); $^6H_{15/2} \rightarrow {}^4I_{13/2}$, $^4F_{7/2}$(387 nm); $^6H_{15/2} \rightarrow {}^4G_{11/2}$(427 nm) and $^6H_{15/2} \rightarrow {}^4I_{15/2}$(453 nm) transitions.[45,46] Hence, one can conclude that the synthesised phosphor shows potential for applications in near-Ultraviolet chips.

The photoluminescence (PL) emission spectra of $Na_3Ba_2LaNb_{10}O_{30}$:xDy^{3+} ($x = 1, 3, 5, 7$ and 10 mol%) phosphors taken in the range of 400–700 nm while keeping excitation wavelength fixed at 387 nm are presented in Fig. 12. The emission spectra shows three characteristic bands centred at 481, 575 and
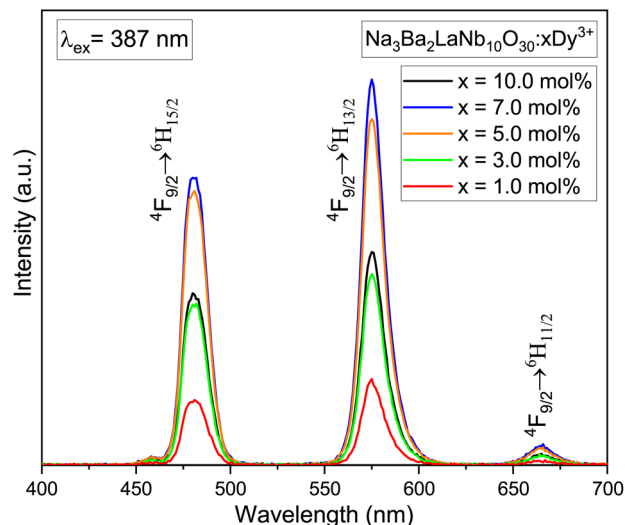

Fig. 12 PL emission spectra of $Na_3Ba_2LaNb_{10}O_{30}$:xDy^{3+} ($x = 1, 3, 5, 7$ and 10 mol%) phosphors under the excitation wavelength of 387 nm.

666 nm which correspond to blue ($^4F_{9/2} \rightarrow {}^6H_{15/2}$ transition), yellow ($^4F_{9/2} \rightarrow {}^6H_{13/2}$ transition) and red ($^4F_{9/2} \rightarrow {}^6H_{11/2}$ transition) respectively. Further, due to magnetic dipole nature of the $^4F_{9/2} \rightarrow {}^6H_{15/2}$ transition the surrounding crystal field lays no effect on it. Whereas, the forced electric dipole $^4F_{9/2} \rightarrow {}^6H_{13/2}$ transition of Dy^{3+} ion is sensitive to surrounding environment. Moreover the intensity of the yellow band is greater than the blue band signifying that the Dy^{3+} ions are present at the sites lacking inversion center in the host lattice.[47,48] The optimized Dy^{3+} ion concentration is 7.0 mol%, beyond which the concentration quenching begins.

3.6 Nephelauxetic ratio (β) and bonding parameter (δ)

To understand the behaviour of ligand field that surrounds the Dy^{3+} ions in the host matrix and to determine the nature of bonding, the (β) and (δ) are evaluated using the following expression:[49]

$$\beta = \frac{\vartheta_c}{\vartheta_a} \quad \text{and} \quad \delta = \frac{1 - \overline{\beta}}{\overline{\beta}} \quad (5)$$

where, ϑ_c and ϑ_a are the wavenumbers in cm^{-1} for a specific transition of RE ion and the same transition of an aqua ion respectively and β represents the average value of all β. Nephelauxetic effect occurs because of the partially filled f-shell. When host matrix is incorporated with RE ions, the 4f shell gets deformed due to the influence of ligand field. The calculated values of β for $Na_3Ba_2LaNb_{10}O_{30}:xDy^{3+}$ ($x = 1, 3, 5, 7$ and 10 mol%) are shown in Table 2.

The δ value strongly relate to the ligand field environment around the Dy^{3+} ions. The value may be positive/negative indicating ionic/covalent nature. The calculated values of δ for $Na_3Ba_2LaNb_{10}O_{30}:xDy^{3+}$ ($x = 1, 3, 5, 7$ and 10 mol%) are shown in Table 2. The positive value indicates that the bond present between Dy–O is covalent in nature,[50] which increases with the increase in Dy^{3+} ions concentration.

3.7 Effect of dysprosium doping concentration

The emission spectra of $Na_3Ba_2LaNb_{10}O_{30}:xDy^{3+}$ ($x = 1, 3, 5, 7$ and 10 mol%) in Fig. 12 showed the same peak positions for all the Dy^{3+} ions concentration. Fig. 13 shows the yellow and blue peak emission intensity of $Na_3Ba_2LaNb_{10}O_{30}:Dy^{3+}$ phosphor with change in Dy^{3+} ion concentration. Fig. 13 reveals that the emission intensity depends upon the concentration of Dy^{3+} ion, and is seen to increase with steady increase in the latter upto 7 mol%. Beyond 7 mol% of Dy^{3+} ion concentration, the luminescence intensity in $Na_3Ba_2LaNb_{10}O_{30}$ phosphor begins to decrease due to quenching of the concentration. This supported the fact that as Dy^{3+} ion concentration increases beyond a certain value, here 7 mol%, the non-radiative energy transfer probability between dysprosium ions tends to increase. Theoretically, the critical distance (R_c) between Dy^{3+} ions after which concentration quenching begins can be calculated using the Blasse formula:[51]

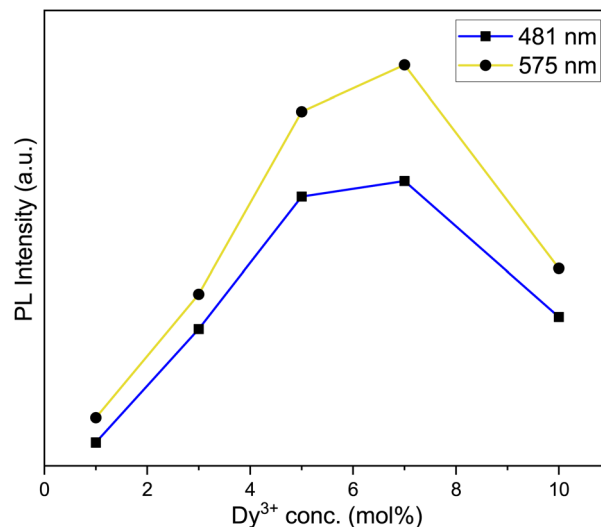$$R_c = 2\left(\frac{3V}{4\pi\chi_c N}\right)^{1/3} \quad (6)$$

Fig. 13 Variation of emission intensity of the emission peaks to various Dy^{3+} ions concentration.

where V denotes the unit cell volume, N denotes the number of cation sites in the host unit cell and χ_c represents the fraction of activator concentration at which quenching occurs. For $Na_3Ba_2LaNb_{10}O_{30}:Dy^{3+}$ phosphor, $\chi_c = 0.07$, $N = 1$, $V = 604.4425$ Å, hence R_c can be calculated as 25.45 Å. Resonant energy transfer is primarily caused by exchange and multipolar interactions. The distance between the adjacent Dy^{3+} ions falls below the critical distance beyond the 7 mol% concentration of Dy^{3+} ions. Given that the calculated R_c value is greater than 5 Å, the multipolar interactions will be dominant in the concentration quenching of $Na_3Ba_2LaNb_{10}O_{30}:Dy^{3+}$ phosphor as the probability of energy transfer via exchange interaction mechanism is very low.[52]

In line with Dexter's hypothesis,[53] type of multipolar interaction mechanism between $Dy^{3+}–Dy^{3+}$ ions can be obtained using the eqn (7).

$$\frac{I}{x} = K\left[1 + \beta(x)^{Q/3}\right]^{-1} \quad (7)$$

here β and K denote constants specific to the host lattice, x represents the activator ion concentration, and I denotes the photoluminescence emission intensity. The Q value defines the multipolarity of electric interaction between the adjacent activator ion.[54] The multipolar character function Q can take values of 3, 6, 8 and 10 according to the interaction mechanism being nearest neighbour, dipole–dipole (d–d), dipole–quadrupole (d–q) and quadrupole–quadrupole (q–q) respectively.[55] The eqn (7) can be approximated to:

$$\log\frac{I}{x} = K' - \frac{Q\log(x)}{3}; \quad \text{here } \left(K' = \log K - \log\beta\right) \quad (8)$$

The linear dependance of $\log(I/x)$ and $\log(x)$ was analysed using $^4F_{9/2}$ transition of dysprosium ion and is shown in Fig. 14. The calculated slope value prior to linear fit is -1.70753, which gives the Q value equivalent to 5.13 (close to 6). Thus, it can be stated that the main mechanism through which energy transfer
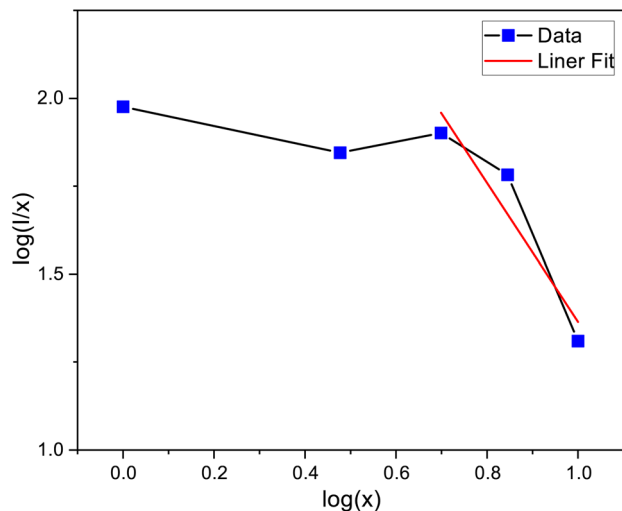
Fig. 14 The linear fitting plot between $\log(I/x)$ and $\log(x)$.

occurs between the adjacent dysprosium ions is dipole–dipole interaction.

The partial energy states of $Na_3Ba_2LaNb_{10}O_{30}:Dy^{3+}$ phosphor is drawn in Fig. 15. The synthesized phosphor absorbs near ultraviolet light corresponding to it's absorption band originating from $^6H_{15/2}$ (ground state) to different excited states. The phosphor $Na_3Ba_2LaNb_{10}O_{30}:Dy^{3+}$ gets excited at 387 nm to populate the short-lived $^4I_{13/2}$ and $^4F_{7/2}$ excited state. The excited ions undergo multiphonon non-radiative transitions to relax to the low lying metastable $^4F_{9/2}$ state. Since beyond this level, the energy spacing between various energy levels is negligible, hence the energy transfer mainly occurs through the non-radiative transitions. The rate of phonon emission (w) can be determined using eqn (9):

$$w = e^{KE/h\nu_{max}} \quad (9)$$

where K is the Boltzmann constant, E is the energy gap and $h\nu_{max}$ is the maximum energy of phonons.

Because of significant energy difference between $^4F_{9/2}$ level and $^6H_{15/2}$, $^6H_{13/2}$, $^6H_{11/2}$ levels, radiative photonic emission

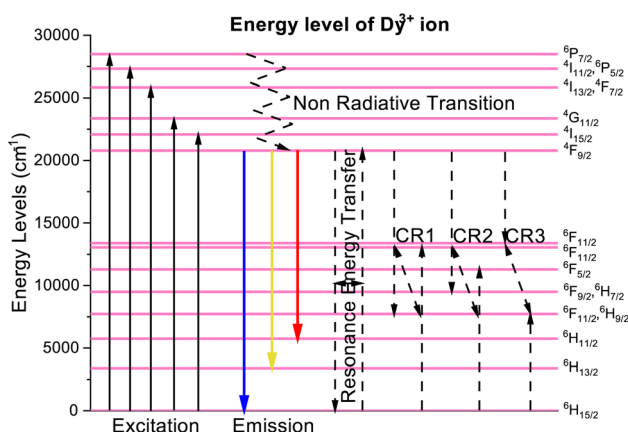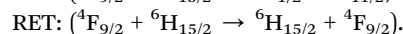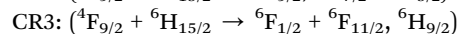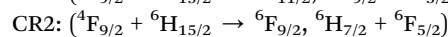takes place. Cross relaxation (CR) channels and resonance energy transfer (RET) between nearby dysprosium ions may be responsible for the non-radiative energy transfer and concentration quenching. According to the energy match rule, the three cross-relaxation channels (CR1, CR2, and CR3) and potential resonant energy transfer are as follows:[50,56,57]

CR1: $(^4F_{9/2} + {}^6H_{15/2} \rightarrow {}^6F_{11/2}, {}^6H_{9/2} + {}^6F_{3/2})$
CR2: $(^4F_{9/2} + {}^6H_{15/2} \rightarrow {}^6F_{9/2}, {}^6H_{7/2} + {}^6F_{5/2})$
CR3: $(^4F_{9/2} + {}^6H_{15/2} \rightarrow {}^6F_{1/2} + {}^6F_{11/2}, {}^6H_{9/2})$
RET: $(^4F_{9/2} + {}^6H_{15/2} \rightarrow {}^6H_{15/2} + {}^4F_{9/2})$.
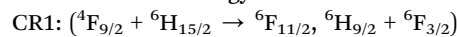
3.8 CIE chromaticity coordinate

CIE chromaticity[58] coordinates were calculated and plotted on CIE 1931 chromaticity diagram, as shown in Fig. 16, using the emission spectra of $Na_3Ba_2LaNb_{10}O_{30}:Dy^{3+}$ phosphors. Here, x and y correspond to the chromaticity coordinates in the CIE 1931 and were obtained as follows:

$$x = \frac{X}{X + Y + Z}, \quad y = \frac{Y}{X + Y + Z} \quad (10)$$

where X, Y, Z are the tristimulus values for the three primary colors $i.e.$ red, green and blue, respectively. The calculated CIE coordinates are found to be quite close to the center white light point (0.33333, 0.33333), as observed in Fig. 16. Correlated color temperature (CCT)[59] relate its color to the color of the light emitted by the black body at a particular temperature, and is measured in Kelvins. Based on the CCT, the phosphors fall in the warm white light region. McCamy's empirical formula[60] was employed to calculate the CCT as stated in the eqn (11):

$$CCT = -449n^3 + 3525n^2 - 6823.3n + 5520.33 \quad (11)$$

where $(x_e = 0.332, y_e = 0.186)$ is the epicenter and $n = \frac{x - x_e}{y - y_e}$ is the inverse slope line.

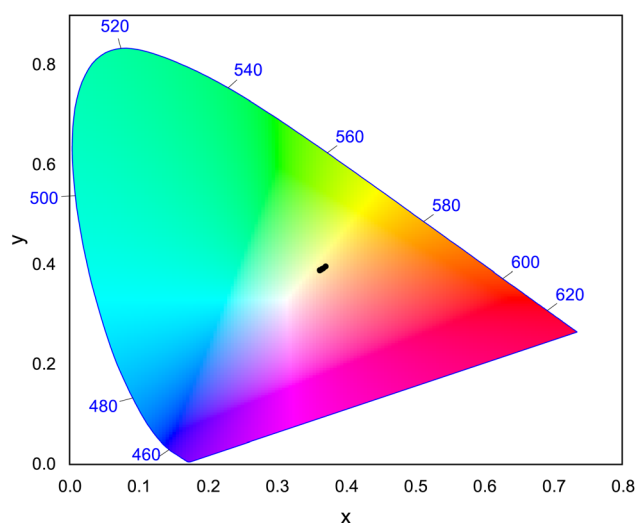**Fig. 15** Partial energy level diagram of Dy^{3+} in $Na_3Ba_2LaNb_{10}O_{30}$ phosphor.

Fig. 16 CIE 1931 chromaticity diagram showing the color coordinates of $Na_3Ba_2LaNb_{10}O_{30}:xDy^{3+}$ ($x = 1, 3, 5, 7$ and 10 mol%) phosphors.

Furthermore, the asymmetry ratio *i.e.* Y/B ratio is the relative measure of band intensities at 575 nm and 481 nm that is used to assess the effectiveness of Dy^{3+} ion doped phosphors. The asymmetry ratio is found close to 1, indicating the appropriate white emission for as prepared Dy^{3+} ion doped phosphor.[61] The Y/B ratio for this investigation lies in the range of 1.18329 to 1.34318 as shown in Table 3. With the increase in Dy^{3+} ion concentration, the position of peak remains unaffected. The color purity of the prepared $Na_3Ba_2LaNb_{10}O_{30}:xDy^{3+}$ ($x = 1, 3, 5, 7$ and 10 mol%) phosphor are calculated using the following formula:

$$\text{Color purity} = \sqrt{\frac{(x - x_i)^2 + (y - y_i)^2}{(x_d - x_i)^2 + (y_d - y_i)^2}} \times 100\% \quad (12)$$

where (x, y) denotes the CIE coordinates of the prepared phosphors, (x_d, y_d) denotes the dominant wavelength coordinates corresponding to the dominant wavelength (λ_d), and (x_i, y_i) denotes the CIE coordinates of the reference white light. The color purity for the prepared samples are calculated between 19% and 24%. The low color purity value is the evident aspect indicating the purity for white light emission which is significantly lower than the previously indicated Dy^{3+} doped phosphors.[62,63] CIE coordinates, CCT, Y/B ratio and color purity are shown in Table 3.

3.9 Lifetime analysis

The phenomenon responsible for the longer decay time is illustrated systematically in the Fig. 17. The Dy^{3+} ion happens to be a potent trap creating ion, and formation of these traps is a major cause for longer decay time. Moreover, the phosphor's luminescence intensity is influenced by the densities of the trapped electrons, whereas its duration is influenced by the depth of the trapped electrons. Phosphor materials when exposed to radiation, cause excitation of the charge carriers and they shift to a higher energy conduction band through process 1 illustrated in Fig. 17. There are two possible choices for these charge carriers to occupy the luminescence centres made by Dy^{3+} ions. One way is for the charge carriers to directly approach the luminescence centres *via* host conduction band (as directed by process 2). However, a fraction of the excited charge carriers get confined into electron traps (as directed by process 3), eventually storing some part of excitation energy. These trapped electrons do not come to the ground state directly, instead they are released from these traps, due to thermal excitations at
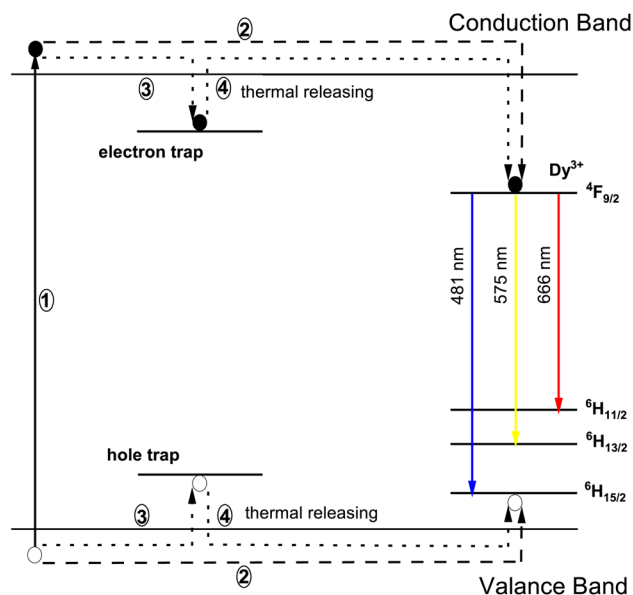

Fig. 17 Schematic diagram of the mechanism in $Na_3Ba_2LaNb_{10}O_{30}:Dy^{3+}$ phosphor.

proper temperature, and get transferred to the luminescent centres *via* host lattice. At these luminescent centres, Dy^{3+} characteristic emissions are observed (as directed by process 4). In physical systems, number of electron and hole traps may not be exactly equal and this embodies the cause for the characteristic luminescence.[64]

The typical luminous decay curve of $Na_3Ba_2LaNb_{10}O_{30}:xDy^{3+}$ ($x = 7$ mol%) phosphor is presented in Fig. 18. The decay curve to calculate lifetime, for $^4F_{9/2} \rightarrow {}^6H_{13/2}$ transition under 487 nm excitation, at room temperature for different Dy^{3+} concentrations, is demonstrated in Fig. 19. It can be seen that, the decay curves fit closely with the double exponential function[65,66] shown in eqn (13). The degree of fitting (χ^2) was observed to be very close to 1 ($\sim$0.99932).

$$I(t) = I_0 + A_1 \exp\left(-\frac{t}{\tau_1}\right) + A_2 \exp\left(-\frac{t}{\tau_2}\right) \quad (13)$$

where I_0 and $I(t)$ signify the phosphorescence intensities at time $t = 0$ and some later time t, respectively. A_1 and A_2 are fitting constants and τ_1 and τ_2 are rapid and slow decay lifetimes. τ_{avg} for different Dy^{3+} doped $Na_3Ba_2LaNb_{10}O_{30}$ phosphors were calculated using eqn (14):[67]

Table 3 CIE coordinate, correlated color temperature, Y/B ratio and average decay time for $Na_3Ba_2LaNb_{10}O_{30}:xDy^{3+}$ ($x = 1, 3, 5, 7$ and 10 mol%) phosphors

Dy^{3+} (mol%)	CIE coordinate		CCT (K)	Y/B ratio	Color purity	Average decay time (μs)
	x	y				
1.0	0.36724	0.39237	4455.777	1.322	23.001	302.559 ± 0.859
3.0	0.36210	0.38917	4585.400	1.183	19.645	249.539 ± 0.906
5.0	0.36695	0.39261	4464.850	1.263	22.842	242.453 ± 1.164
7.0	0.37063	0.39636	4383.463	1.343	25.364	238.778 ± 2.054
10.0	0.36496	0.39091	4512.177	1.240	21.508	207.428 ± 3.567
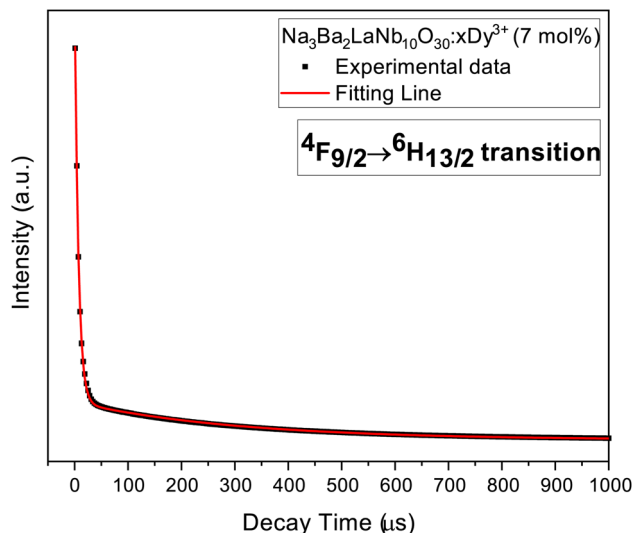
Fig. 18 Decay curve $4F_{9/2} \rightarrow 6H_{13/2}$ transition in $Na_3Ba_2LaNb_{10}O_{30}$:-xDy^{3+} (x = 7 mol%) phosphor.

$$\tau_{\mathrm{avg}} = \frac{A_1 \tau_1^2 + A_2 \tau_2^2}{A_1 \tau_1 + A_2 \tau_2} \quad (14)$$

Table 3 summarises the average decay time τ_{avg} of different Dy^{3+} doped $Na_3Ba_2LaNb_{10}O_{30}$ phosphors. It is clearly evident that as the Dy^{3+} ion concentration increases, the τ_{avg} of the prepared phosphors gradually decreases from 302.6 μs to 207.4 μs because of energy transfer between adjacent Dy^{3+} ions.

3.10 Internal quantum yield (IQE) and brightness (B)

Internal quantum yield (IQE) is an important aspect of a phosphor as it gives the efficiency of conversion of electrical power to observed optical power. The IQE of $Na_3Ba_2LaNb_{10}O_{30}$:xDy^{3+} (x = 7 mol%) phosphor, shown in Fig. 20, was measured using the reference of $BaSO_4$ excitation line. Qualitatively, IQE is the ratio
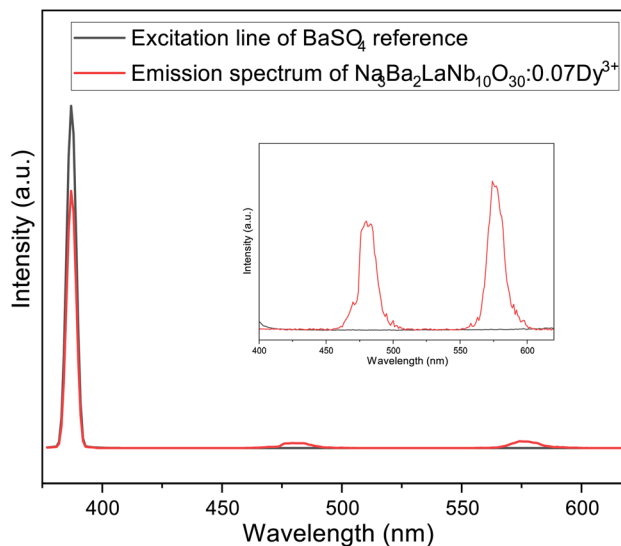

Fig. 19 Decay curves for $4F_{9/2} \rightarrow 6H_{13/2}$ transition in $Na_3Ba_2LaNb_{10}$-O_{30}:xDy^{3+} (x = 1, 3, 5, 7 and 10 mol%) phosphors.

Fig. 20 Excitation and emission spectra of $Na_3Ba_2LaNb_{10}O_{30}$:xDy^{3+} (x = 7 mol%) phosphor and $BaSO_4$ reference using an integrating sphere for IQE measurement. Inset: enlarged emission spectra (400–630 nm).

of number of emitted and absorbed photons and can be obtained using the eqn (15):[68]

$$\eta = \frac{\int L_S}{\int E_R - \int E_S} \quad (15)$$

where η represents IQE, L_S denotes to the emission spectra of $Na_3Ba_2LaNb_{10}O_{30}$:xDy^{3+} (x = 7 mol%), E_S represent phosphor excitation spectra and E_R represent excitation exclusively with $BaSO_4$ as reference. IQE (η) of $Na_3Ba_2LaNb_{10}O_{30}$:xDy^{3+} (x = 7 mol%) phosphor was calculated as 45.35% under the excitation of 387 nm, which is significantly higher than previously reported $Ca_2ZnSi_2O_7$:Dy^{3+},Eu^{3+} (IQE: 12.88%),[69] $LiCaBO_3$:Dy^{3+} (IQE: 25.00%)[70] and $Ca_2NaMg_2V_3O_{12}$:Dy^{3+} (IQE: 25.00%)[71] phosphors. Similarly, brightness (B)[72] is a dimensionless quantity defined as a parameter that has nothing to do with how sensitive the human eye is and is defined by eqn (16):

$$B = \frac{n_e}{n_i} = \frac{n_e}{n_a} \times \frac{n_a}{n_i} = \eta \times \xi_{\mathrm{abs}} \quad (16)$$

where n_a, n_i and n_e correspond to the number of photons absorbed, incident and emitted respectively. Hence absorption efficiency ξ_{abs} becomes:

$$\xi_{\mathrm{abs}} = \frac{n_a}{n_i} \quad (17)$$

The calculated value of brightness for $Na_3Ba_2LaNb_{10}O_{30}$:-xDy^{3+} (x = 7 mol%) phosphors is 11.41%.

4   Conclusions

In this study, a series of novel white light emitting dysprosium doped $Na_3Ba_2LaNb_{10}O_{30}$ phosphors were successfully

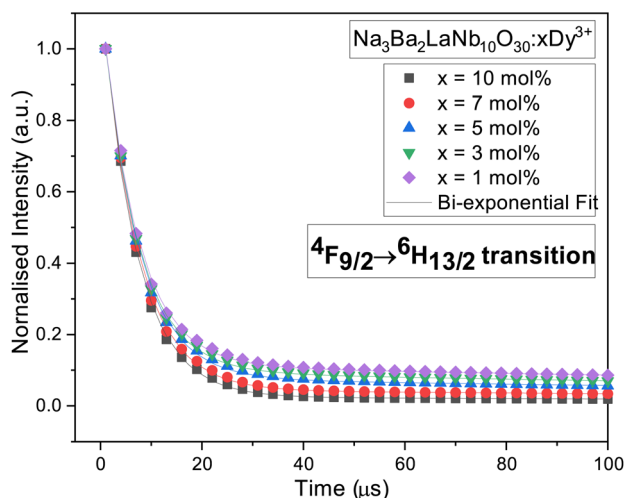synthesized through conventional solid-state reaction method. Their structural, morphological, and spectroscopic properties have been investigated for w-LED application using XRD, FE-SEM, FT-IR, steady state and time resolved spectroscopy and quantum yield. X-ray diffractometer confirms that the prepared phosphors were in pure phase, and the crystal system is revealed as filled TTB with $P4bm$ space group. The FE-SEM micrograph reveals that the particle size distribution is in both μm and nm ranges, and the agglomerated particles were of non-uniform shape. Raman and FT-IR spectra indicates the presence of different vibrational modes and functional groups, respectively. Ultraviolet visible diffuse reflectance spectra (UV-DRS) indicates the presence of surface defects in the prepared phosphors. The phosphor emits white light under near-ultraviolet (n-UV) excitation via a dominant mix of blue and yellow emission bands at 481 nm ($^4F_{9/2} \rightarrow {}^6H_{15/2}$) and 575 nm ($^4F_{9/2} \rightarrow {}^6H_{13/2}$), respectively. The optimised concentration of Dy^{3+} ions beyond which quenching occurs was found to be 7.0 mol%. This concentration quenching mechanism arises due to dipole–dipole interaction. Nephelauxetic ratio and bonding parameters were determined from their luminescent spectra. The CIE chromaticity coordinates, CCT, Y/B ratio and color purity indicates that the synthesised phosphors emits warm white light. The decay time decreases with increasing concentration of Dy^{3+} ions due to energy transfer between neighbouring Dy^{3+} ions, as indicated by the lifetime decay curves. The Internal Quantum Yield and Brightness calculated for the optimised phosphor suggests that the prepared phosphor has a potential utility in w-LED application under n-UV excitation.

Author contributions

Kanishk Poria: conceptualization, methodology, writing – original draft. Ravina: conceptualization, methodology, writing – original draft. Sanjana Bhatia: data curation, writing, review, editing. Amit Kumar: formal analysis. Rajwinder Singh: formal analysis. Nisha Deopa: supervision, methodology, software, validation, writing, review, editing, formal analysis. Rajesh Punia: resources. Jangvir Singh Shahi: supervision, methodology, software, validation, writing, review, editing, formal analysis. A. S. Rao: resources, formal analysis.

Conflicts of interest

There are no conflicts to declare.

Acknowledgements

References

1 H. Hu and W. Zhang, *Opt. Mater.*, 2006, **28**, 536–550.

2 M. Djamal, L. Yuliantini, R. Hidayat, K. Boonin, P. Yasaka and J. Kaewkhao, *Mater. Today: Proc.*, 2018, **5**, 15126–15130.

3 L. Fan, Y. Shi, Y. Wu, J. Xie, J. Zhang, F. Lei and L. Zhang, *J. Lumin.*, 2017, **190**, 504–510.

4 S. Verma, K. Verma, D. Kumar, B. Chaudhary, S. Som, V. Sharma, V. Kumar and H. C. Swart, *Phys. B Condens. Matter*, 2018, **535**, 106–113.

5 Y. Liu, R. Wang, Q. Yang, G. Li, J. Huang and G. Cai, *J. Am. Ceram. Soc.*, 2022, **105**, 6184–6195.

6 Y. Liu, X. Liu, W. Wang, B. Zhou and Q. Zhang, *Mater. Res. Bull.*, 2017, **95**, 235–242.

7 N. Deopa, A. Rao, M. Gupta and G. V. Prakash, *Opt. Mater.*, 2018, **75**, 127–134.

8 T. Pulli, T. Dönsberg, T. Poikonen, F. Manoocheri, P. Kärhä and E. Ikonen, *Light Sci. Appl.*, 2015, **4**, e332.

9 M.-H. Fang, C. Ni, X. Zhang, Y.-T. Tsai, S. Mahlik, A. Lazarowska, M. Grinberg, H.-S. Sheu, J.-F. Lee, B.-M. Cheng, et al., *ACS Appl. Mater. Interfaces*, 2016, **8**, 30677–30682.

10 J. Chen, Y. Liu, L. Mei, H. Liu, M. Fang and Z. Huang, *Sci. Rep.*, 2015, **5**, 1–9.

11 X. Chen, P. Dai, X. Zhang, C. Li, S. Lu, X. Wang, Y. Jia and Y. Liu, *Inorg. Chem.*, 2014, **53**, 3441–3448.

12 K. Jha, A. K. Vishwakarma, M. Jayasimhadri and D. Haranath, *J. Alloys Compd.*, 2017, **719**, 116–124.

13 K. Shinde and S. Dhoble, *Crit. Rev. Solid State Mater. Sci.*, 2014, **39**, 459–479.

14 M. Shi, L. Yao, J. Xu, C. Liang, Y. Dong and Q. Shao, *J. Am. Ceram. Soc.*, 2021, **104**, 3279–3288.

15 P. Dang, G. Li, X. Yun, Q. Zhang, D. Liu, H. Lian, M. Shang and J. Lin, *Light Sci. Appl.*, 2021, **10**, 1–13.

16 M. Tshabalala, F. Dejene, S. S. Pitale, H. Swart and O. Ntwaeaborwa, *Phys. B Condens. Matter*, 2014, **439**, 126–129.

17 N. Lakshminarasimhan and U. Varadaraju, *J. Electrochem. Soc.*, 2005, **152**, H152.

18 G. Hu, S. Yi, Z. Fang, Z. Hu and W. Zhao, *Opt. Mater.*, 2019, **98**, 109428.

19 F. Xiong, F. Xu, H. Lin, Y. Wang, E. Ma and W. Zhu, *Appl. Phys. A*, 2020, **126**, 1–8.

20 Z. Li, Y. Hua and G. Ou, *Optik*, 2021, **233**, 166595.

21 P. Wang, L. Schwertmann, R. Marschall and M. Wark, *J. Mater. Chem. A*, 2014, **2**, 8815–8822.

22 Y. Ma, R. Liu, X. Geng, X. Hu, W. Chen, B. Deng, R. Yu and H. Geng, *Ceram. Int.*, 2022, **48**, 4080–4089.

23 G. Zhu, Z. Ci, S. Xin, Y. Wen and Y. Wang, *Mater. Lett.*, 2013, **91**, 304–306.

24 T. Wei, Y. Wang, Q. Zhou, Z. Li, L. Zhan and Q. Jin, *Ceram. Int.*, 2014, **40**, 16647–16651.

25 C.-J. Chan, F. F. Lange, M. Rühle, J.-F. Jue and A. V. Virkar, *J. Am. Ceram. Soc.*, 1991, **74**, 807–813.

26 R. Jain, R. Sinha, M. K. Sahu and M. Jayasimhadri, *J. Lumin.*, 2021, **36**, 1444–1451.

27 B. M. Mothudi, O. Ntwaeaborwa, S. S. Pitale and H. Swart, *J. Alloys Compd.*, 2010, **508**, 262–265.

28 P. Babu, K. H. Jang, E. S. Kim, L. Shi, H. J. Seo and F. Lopez, *J. Korean Phys. Soc.*, 2009, **54**, 1488–1491.

29 S. K. Gupta, M. Kumar, V. Natarajan and S. Godbole, *Opt. Mater.*, 2013, **35**, 2320–2328.

30 M. K. Sahu and J. Mula, *J. Am. Ceram. Soc.*, 2019, **102**, 6087–6099.

31 L. Fang, H. Zhang, J. Yang, F. Meng and R. Yuan, *J. Mater. Sci. Lett.*, 2003, **22**, 1705–1707.

32 L. Sun, B. Devakumar, J. Liang, B. Li, S. Wang, Q. Sun, H. Guo and X. Huang, *RSC Adv.*, 2018, **8**, 31835–31842.

33 L. Alexander and H. P. Klug, *J. Appl. Phys.*, 1950, **21**, 137–142.

34 K. Rawat and P. Shishodia, *Adv. Powder Technol.*, 2017, **28**, 611–617.

35 M. Bouziane, M. Taibi, L. Saviot and A. Boukhari, *Phys. B Condens. Matter*, 2011, **406**, 4257–4260.

36 R. E. Wilde, *J. Raman Spectrosc.*, 1991, **22**, 321–325.

37 A. Boudou and J. Sapriel, *Phys. Rev. B: Condens. Matter Mater. Phys.*, 1980, **21**, 61.

38 S. Jana, A. Mondal, J. Manam and S. Das, *J. Alloys Compd.*, 2020, **821**, 153342.

39 H. Kabir, S. H. Nandyala, M. M. Rahman, M. A. Kabir and A. Stamboulis, *Appl. Phys. A*, 2018, **124**, 1–11.

40 M. Salavati-Niasari, G. Hosseinzadeh and F. Davar, *J. Alloys Compd.*, 2011, **509**, 134–140.

41 M. Afqir, A. Tachafine, D. Fasquelle, M. Elaatmani, J.-C. Carru, A. Zegzouti, M. Daoud, S. Sayouri, T.-d. Lamcharfi and M. Zouhairi, *Process. Appl. Ceram.*, 2018, **12**, 72–77.

42 H. Bruncková, L. Medveckỳ, P. Hvizdoš, J. Ďurišin and V. Girman, *J. Mater. Sci.*, 2015, **50**, 7197–7207.

43 I. P. Sahu, D. Bisen, N. Brahme and R. K. Tamrakar, *J. Electron. Mater.*, 2016, **45**, 2222–2232.

44 M. Jiao, C. Yang, M. Liu, Q. Xu, Y. Yu and H. You, *Opt. Mater. Express*, 2017, **7**, 2660–2671.

45 W. Carnall, P. Fields and K. Rajnak, *J. Chem. Phys.*, 1968, **49**, 4424–4442.

46 K. Poria, N. Deopa and J. S. Shahi, *Laser Sci.*, 2022, JW5A.1.

47 Q. Su, Z. Pei, L. Chi, H. Zhang, Z. Zhang and F. Zou, *J. Alloys Compd.*, 1993, **192**, 25–27.

48 L. Mishra, A. Sharma, A. K. Vishwakarma, K. Jha, M. Jayasimhadri, B. Ratnam, K. Jang, A. Rao and R. Sinha, *J. Lumin.*, 2016, **169**, 121–127.

49 C. Jorgensen, *Prog. Inorg. Chem.*, 1962, **4**, 73–124.

50 N. Deopa and A. Rao, *J. Lumin.*, 2017, **192**, 832–841.

51 G. Blasse, *Phys. Lett. A*, 1968, **28**, 444–445.

52 L. Van Uitert, *J. Electrochem. Soc.*, 1967, **114**, 1048.

53 D. L. Dexter and J. H. Schulman, *J. Chem. Phys.*, 1954, **22**, 1063–1070.

54 D. L. Dexter, *J. Chem. Phys.*, 1953, **21**, 836–850.

55 S. Kaur, A. Rao and M. Jayasimhadri, *Ceram. Int.*, 2017, **43**, 7401–7407.

56 A. K. Vishwakarma, K. Jha, M. Jayasimhadri, B. Sivaiah, B. Gahtori and D. Haranath, *Dalton Trans.*, 2015, **44**, 17166–17174.

57 J. S. Kumar, K. Pavani, A. M. Babu, N. K. Giri, S. Rai and L. R. Moorthy, *J. Lumin.*, 2010, **130**, 1916–1923.

58 F. Miller, A. Vandome and M. John, *CIE 1931 Color Space*, VDM Publishing, 2010.

59 M. N. Khan, *Understanding LED illumination*, CRC Press, 2013.

60 C. S. McCamy, *Color Res. Appl.*, 1992, **17**, 142–144.

61 B. Ratnam, M. Jayasimhadri, K. Jang, H. Sueb Lee, S.-S. Yi and J.-H. Jeong, *J. Am. Ceram. Soc.*, 2010, **93**, 3857–3861.

62 P. Nayak, S. S. Nanda, S. K. Gupta, K. Sudarshan and S. Dash, *J. Am. Ceram. Soc.*, 2022, **105**, 7384–7398.

63 S. Sharma, N. Brahme, D. Bisen and P. Dewangan, *Opt. Express*, 2018, **26**, 29495–29508.

64 I. P. Sahu, D. Bisen and N. Brahme, *Displays*, 2014, **35**, 279–286.

65 K. Li, X. Liu, Y. Zhang, X. Li, H. Lian and J. Lin, *Inorg. Chem.*, 2015, **54**, 323–333.

66 K. Jha and M. Jayasimhadri, *J. Am. Ceram. Soc.*, 2017, **100**, 1402–1411.

67 J. Sun, X. Zhang, Z. Xia and H. Du, *Mater. Res. Bull.*, 2011, **46**, 2179–2182.

68 S. Wang, Y. Xu, T. Chen, W. Jiang, J. Liu, X. Zhang, W. Jiang and L. Wang, *Chem. Eng. J.*, 2021, **404**, 125912.

69 K. Mondal and J. Manam, *J. Lumin.*, 2018, **195**, 259–270.

70 A. R. Beck, S. Das and J. Manam, *J. Mater. Sci.: Mater. Electron.*, 2017, **28**, 17168–17176.

71 L. Yang, X. Mi, H. Zhang, X. Zhang, Z. Bai and J. Lin, *J. Alloys Compd.*, 2019, **787**, 815–822.

72 P. A. Tanner, L. Zhou, C. Duan and K.-L. Wong, *Chem. Soc. Rev.*, 2018, **47**, 5234–5265.